An Isoparametric Tangled Finite Element Method for Handling Higher-order Elements with Negative Jacobian

Bhagyashree Prabhune, Krishnan Suresh*

Department of Mechanical Engineering, University of Wisconsin-Madison, WI, USA

Abstract

This paper presents an isoparametric tangled finite element method (i-TFEM) method for handling *tangled* high order/curvilinear meshes. Tangled elements, i.e. elements with negative Jacobian determinant, frequently occur during various stages of analysis and optimization, leading to erroneous results in standard finite element method (FEM). The proposed i-TFEM is an extension of standard FEM to allow for tangled elements. Specifically, a novel variational formulation is proposed that leads to a simple modification of the standard FEM stiffness matrix and additional piece-wise compatibility constraints. Moreover, i-TFEM reduces to the standard FEM for non-tangled (regular) meshes. The accuracy of the proposed i-TFEM is demonstrated for tangled 9-node quadrilateral (Q9) and 6-node triangular (T6) elements. Numerical experiments involving linear and nonlinear elasticity and Poisson problems illustrate that the accuracy and convergence rate of the proposed i-TFEM over a tangled mesh is comparable to that of the standard FEM over a non-tangled mesh.

Keywords: Tangled Mesh, Negative Jacobian, Higher order, Mixed finite element, Algebraic constraints

1. Introduction

Higher-order finite elements typically exhibit higher accuracy and convergence rate at a lower computational cost, compared to their lower-order counterparts [1, 2]. Consequently, they have been deployed in various applications including solid mechanics [3, 4], fluid mechanics [5, 6], electromagnetics [7], coupled problems [8], etc.

In this paper, we consider *tangled* meshes where one or more elements exhibit negative Jacobian, i.e., where the parametric mapping is not fully invertible (the notion of non-invertible mapping is further elaborated in the next section). Specifically, the paper focuses on tangled Q9 and T6 elements, as illustrated in Fig. 1c and Fig. 1d respectively. It is well known that the standard finite element method (FEM) will lead to erroneous results over such meshes [1, 9, 10, 11]. Unfortunately, tangled meshes frequently occur during meshing [12, 13, 14, 15], mesh optimization [16, 17, 18], shape optimization [19, 20] and mesh morphing [21]. To quote [22], *"... challenge in the generation of high-order meshes is mesh tangling."*

*Corresponding author

Email addresses: bprabhune@wisc.edu (Bhagyashree Prabhune), ksuresh@wisc.edu (Krishnan Suresh)

Since tangled meshes have been traditionally considered unacceptable (invalid) for finite element analysis, several mesh untangling [23, 22, 24, 25, 26] techniques have been developed. Many popular mesh generating software with built-in untangling algorithms may fail to untangle the meshes [27]. To quote [27] *"... (meshCurve and Netgen) resulted in tangled meshes which the respective software packages failed to untangle."*

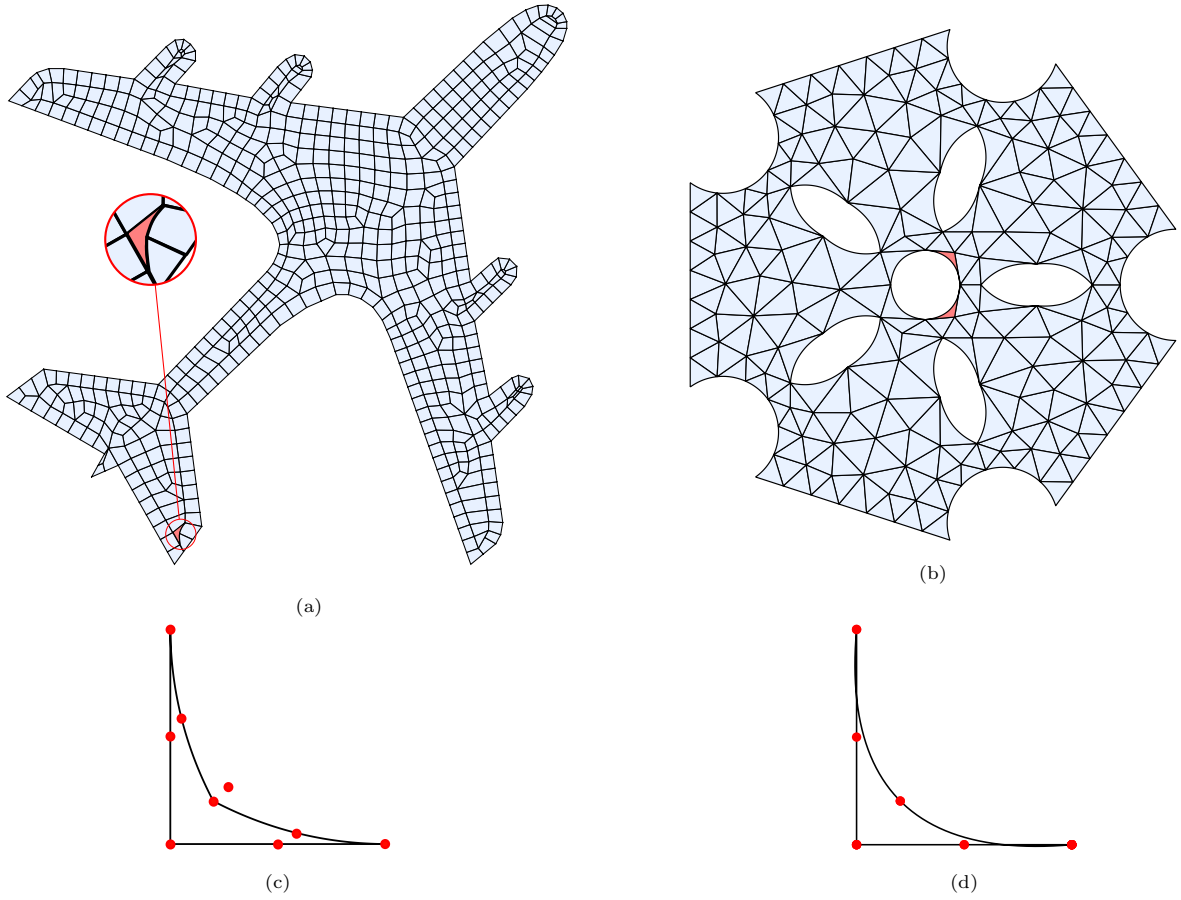

Figure 1: (a) Tangled mesh with 9-node quadrilateral elements; the mesh has been generated using the algorithm presented in [28]; (b) Tangled mesh with 6-node triangular elements; the mesh has been provided by the authors of [22]. Highlighted elements are tangled (negative Jacobian elements). A typical element with negative Jacobian (c) quadrilateral (Q9), and (d) triangular (T6).

Various non-traditional finite element methods have been proposed to handle such tangled elements. Methods such as the smoothed finite element method [29] and virtual element method [30] were initially proposed to handle tangled lower order elements, and later extended to higher order elements [2, 31, 32, 33, 34]. However, they do not reduce to standard FEM for non-tangled (regular) meshes. Unsymmetric finite elements [35] have been proposed to handle tangled higher order elements, but they result in asymmetric stiffness matrices.

Recently an isoparametric tangled finite element method (i-TFEM) framework [36] was proposed to han-

dle tangled 4-node quadrilateral (Q4) and 8-node hexahedral (H8) elements. The method was demonstrated for linear elasticity [36], Poisson [37], incompressibility as well as nonlinear elasticity [38] problems. It was shown that i-TFEM reduces to standard FEM for regular (non-tangled) meshes and produces symmetric stiffness matrices. However, the implementation of i-TFEM discussed in [36] requires integration over non-convex folded regions (that is induced by tangling); this was performed by triangulating the region. For Q4 elements, the folded regions are simple triangles, and therefore the integration can be performed easily. However, for Q9 and T6 elements, the folded regions have curved boundaries, and the integration is computationally expensive since a large number of triangles are needed to achieve high accuracy.

In this paper, we introduce a novel variation of i-TFEM, which makes the implementation simpler, faster, and well-suited for handling higher order elements with curved edges. Specifically, we generalize the i-TFEM method to Q9 and T6 elements through three contributions. The first is to develop a mixed variational formulation based on the stationary potential energy principle with compatibility constraint over the tangled regions. This leads to the second contribution of developing an efficient method to compute the stiffness matrix that does *not* entail integrating over the fold. The third contribution is to also provide a numerically efficient method for constructing the compatibility matrix. Numerical experiments involving linear and nonlinear elasticity as well as Poisson problems demonstrate that i-TFEM can match the accuracy of standard FEM over non-tangled (regular) meshes.

The remainder of this paper is organized as follows. The basic concept underlying i-TFEM is reviewed in Section 2. Then, a variational treatment of i-TFEM for Q9 and T6 elements is presented in Section 3, followed by a detailed description of the implementation in Section 4. Results from numerical experiments are presented in Section 5, and conclusions in Section 6.

2. Background: Isoparametric TFEM

We briefly review critical i-TFEM concepts [36, 39, 37], prior to generalizing these concepts via a variational formulation. Consider the standard mapping ϕ from a parametric (ξ_1, ξ_2) space in Fig. 2a to the tangled (partially inverted) element in the physical space (x_1, x_2) as shown in Fig. 2b. Observe that the mapping is non-invertible; i.e., two points ($\boldsymbol{a}$ and $\boldsymbol{b}$) in the parametric space map to the same point $\boldsymbol{p}$ in the physical space. Visually, the element folds onto itself. Further, at points such as $\boldsymbol{a}$, the determinant of the Jacobian is negative, while at $\boldsymbol{b}$, the determinant is positive. Thus, one can divide the parametric space into positive and negative regions denoted as J^+ and J^- respectively. The procedure to identify the J^+ and J^- regions is discussed in Appendix A. However, it is important to note that identification of the J^+ and J^- regions is *not* required in the proposed i-TFEM formulation (see Section 4).

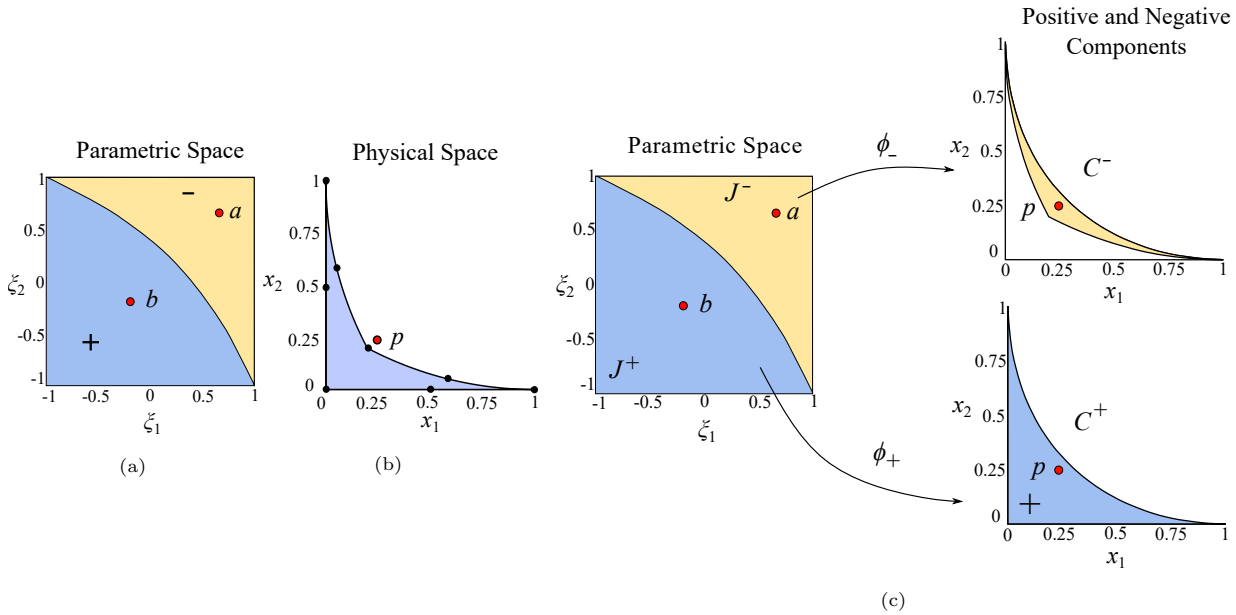

Figure 2: (a) Parametric space of the tangled element. Parametric space can be divided into positive and negative Jacobian regions. (b) Physical space of the tangled Q9 element. (c) Positive and negative components

The main idea in i-TFEM is that the positive and negative Jacobian regions (J^+ and J^-) are treated separately while constructing the stiffness matrix. The corresponding regions in the physical space are referred to here as positive (C^+) and negative (C^-) components respectively (see Fig. 2c). Observe the two independent mappings

$$\phi_{\pm}\colon J^{\pm} \to C^{\pm}$$

are invertible (bijective). Thus, i-TFEM replaces the full-invertibility constraint by partial invertibility.

3. Proposed Method

Now consider the two-element mesh shown in Fig. 3a (the central nodes for the two Q9 elements are not shown to avoid clutter). The positive and negative components of the tangled element E_1 are shown in Fig. 3b. On the other hand, the non-tangled element E_2 has only one positive component (see Fig. 3c): $E_2 = C_2^+$ while $C_2^- = \emptyset$. Further, the fold F_1 illustrated in Fig. 3d overlaps with E_2 as well.

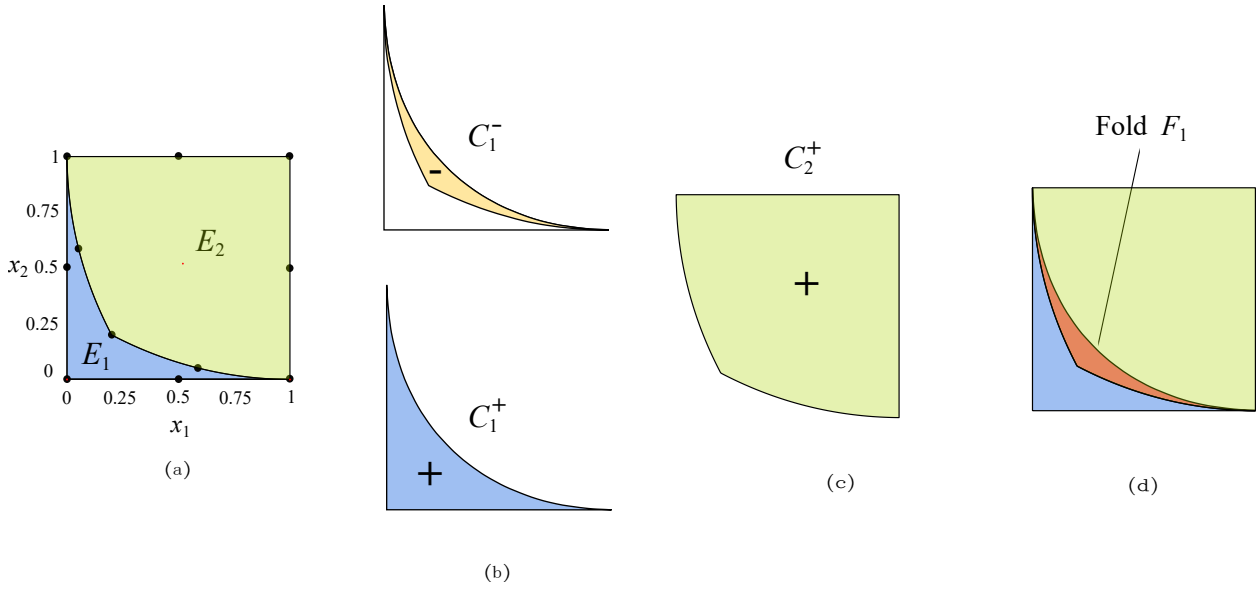

Figure 3: (a) 2-D domain discretized into two 9-node quadrilateral elements (central nodes are not shown to avoid clutter). (b) Positive and negative $|\boldsymbol{J}|$ regions of the tangled element. (c) Non-tangled element of the mesh. (d) Fold overlaps with neighbor.

Let $\boldsymbol{N}_j(\boldsymbol{\xi})$ be the standard biquadratic Lagrange shape functions defined over the parametric space. Let $\boldsymbol{N}_j^{\pm}$ be the restriction of $\boldsymbol{N}_j$ to $J^{\pm}$, i.e.,

$$\boldsymbol{N}_j^{\pm}(\boldsymbol{x}) \coloneqq \boldsymbol{N}_j(\phi_{\pm}^{-1}(\boldsymbol{x})) \tag{1}$$

The corresponding fields are given by

$$u_j^{\pm}(\boldsymbol{x}) = \boldsymbol{N}_j^{\pm}(\boldsymbol{x})\hat{\boldsymbol{u}}_j \tag{2}$$

Since any point $\boldsymbol{x}$ in the fold belongs to three components C_1^+, C_1^-, and C_2^+, one can define three fields $u_1^+(\boldsymbol{x})$, $u_1^-(\boldsymbol{x})$ and $u_2^+(\boldsymbol{x})$. To resolve this ambiguity and to ensure field continuity, a *piecewise compatibility constraint* is enforced over the fold [36]:

$$u_1^+(\boldsymbol{x}) - u_1^-(\boldsymbol{x}) = 0, \quad \forall \boldsymbol{x} \in F_1. \tag{3}$$

Introducing the notation $[\![\cdot]\!] = (\cdot)^+ - (\cdot)^-$, the above constraint can be written as:

$$[\![u_1]\!] = 0, \quad \text{in } F_1. \tag{4}$$

We will now consider solving the Poisson problem over the two-element mesh. Recall that the standard potential energy for the Poisson problem is given by:

$$\Pi = \int_{E_1} \left(\frac{1}{2} (\nabla u_1)^\top \boldsymbol{D} (\nabla u_1) - u_1 b \right) d\Omega + \int_{E_2} \left(\frac{1}{2} (\nabla u_2)^\top \boldsymbol{D} (\nabla u_2) - u_2 b \right) d\Omega - \sum_{j \in 1,2} \int_{\partial E_j^q} u_j q dS \tag{5}$$

where $\boldsymbol{D}$ is the material constitutive matrix, b is the source term, and q is the boundary flux over the boundary ∂E_j^q. We will assume that the field u satisfies the Dirichlet boundary condition $u_j = u_j^d$ over the

boundary ∂E_j^d. The above formulation (used in standard FEM) leads to erroneous results over the tangled mesh (later demonstrated in Section 5). On the other hand, in i-TFEM, positive and negative components are handled separately.

To motivate the concept, observe that the total area of the two-element mesh is given by:

$$A = (A_1^+ - A_1^-) + A_2^+ \tag{6}$$

where,

$$A_1^+ = \int\limits_{C_1^+} d\Omega, \quad A_1^- = \int\limits_{C_1^-} d\Omega, \quad \text{and} \quad A_2^+ = \int\limits_{C_2^+} d\Omega. \tag{7}$$

Observe that all the areas A_1^+, A_1^-, and A_2^+ are positive in value, but the area of the negative component is subtracted from the area of the positive component.

In the same vein, we propose a modified energy functional where the positive and negative components are treated separately and the contribution of the negative component is subtracted. Moreover, the piecewise compatibility constraint (Eq. 4) is incorporated as follows:

$$\begin{aligned}\widetilde{\Pi} = &\int\limits_{C_1^+} \left(\frac{1}{2}\left(\nabla u_1^+\right)^\top \boldsymbol{D}\left(\nabla u_1^+\right) - u_1^+ b\right) d\Omega \; - \int\limits_{C_1^-} \left(\frac{1}{2}\left(\nabla u_1^-\right)^\top \boldsymbol{D}\left(\nabla u_1^-\right) - u_1^- b\right) d\Omega \\ &+ \int\limits_{C_2^+} \left(\frac{1}{2}\left(\nabla u_2^+\right)^\top \boldsymbol{D}\left(\nabla u_2^+\right) - u_2^+ b\right) d\Omega \; - \sum_{j\in 1,2} \int\limits_{\partial E_j^q} u_j q dS + \int\limits_{F_1} \lambda_1 [\![u_1]\!] d\Omega.\end{aligned} \tag{8}$$

Observe that: (1) the first three terms involve integration over the components C_1^+, C_1^-, and C_2^+ respectively, (2) the contribution from the component C_1^- is subtracted since it is a negative component, (3) the fourth term is the standard boundary flux and, (4) the last term incorporates the compatibility constraint over the folds F_1 via Lagrange multiplier field λ_1 (the use of Lagrange multipliers to impose constraints is common in several finite element formulations [40, 41, 42, 43, 44, 45]).

The potential energy (Eq. 8) can be easily generalized for a mesh containing M elements, identified by the set $I = \{1, \ldots, M\}$. Each element E_j has an associated positive C_j^+ component (and a negative component C_j^- if the element is tangled). The tangled elements are identified by the index I_{tangled}. The energy functional can therefore be written as:

$$\begin{aligned}\widetilde{\Pi} = &\sum_{j\in I} \int\limits_{C_j^+} \left(\frac{1}{2}\left(\nabla u_j^+\right)^\top \boldsymbol{D}\left(\nabla u_j^+\right) - u_j^+ b\right) d\Omega \; - \sum_{j\in I_{\text{tangled}}} \int\limits_{C_j^-} \left(\frac{1}{2}\left(\nabla u_j^-\right)^\top \boldsymbol{D}\left(\nabla u_j^-\right) - u_j^- b\right) d\Omega \\ &- \sum_{j\in I} \int\limits_{\partial E_j^q} u_j q dS + \sum_{j\in I_{\text{tangled}}} \int\limits_{F_j} \lambda_j [\![u_j]\!] d\Omega.\end{aligned} \tag{9}$$

Taking the variation with respect to the two fields u and λ, we arrive at the following weak form:

Find $u \in H^1$ and $\lambda \in L^2$ such that

$$a(\delta u, u) + b(\delta u, \lambda) = f(\delta u), \quad \forall \delta u \in H_0^1 \tag{10a}$$

$$b(\delta\lambda, u) = 0, \qquad \forall \delta\lambda \in L^2 \tag{10b}$$

where,

$$a(\delta u, u) = \sum_{j \in I} \int_{C_j^+} \left(\nabla \delta u_j^+\right)^\top \boldsymbol{D} \nabla u_j^+ \, d\Omega - \sum_{j \in I_{\text{tangled}}} \int_{C_j^-} \left(\nabla \delta u_j^-\right)^\top \boldsymbol{D} \nabla u_j^- \, d\Omega$$

$$b(\delta u, \lambda) = \sum_{j \in I_{\text{tangled}}} \int_{F_j} [\![\delta u_j]\!] \lambda_j \, d\Omega \tag{11}$$

$$f(\delta u) = \sum_{j \in I} \int_{C_j^+} \delta u_j^+ b d\Omega - \sum_{j \in I_{\text{tangled}}} \int_{C_j^-} \delta u_j^- b d\Omega + \sum_{j \in I} \int_{\partial E_j^q} \delta u_j q dS. \tag{12}$$

We now approximate the primary field u and the Lagrange multiplier field λ as follows:

$$u_j \approx \boldsymbol{N}_j \hat{\boldsymbol{u}}_j, \quad \lambda_j \approx \boldsymbol{N}^\lambda \hat{\boldsymbol{\lambda}}. \tag{13}$$

Adopting a (Bubnov-) Galerkin method leads to the following system of equations:

$$\begin{bmatrix} \boldsymbol{K} & \boldsymbol{C} \\ \boldsymbol{C}^\top & \boldsymbol{0} \end{bmatrix} \begin{Bmatrix} \hat{\boldsymbol{u}} \\ \hat{\boldsymbol{\lambda}} \end{Bmatrix} = \begin{Bmatrix} \boldsymbol{f} \\ \boldsymbol{0} \end{Bmatrix} \tag{14}$$

where the stiffness matrix is given by:

$$\boldsymbol{K} = \prod_{j \in I} \int_{C_j^+} \left(\nabla \boldsymbol{N}_j^{+\top} \boldsymbol{D} \nabla \boldsymbol{N}_j^+\right) d\Omega \quad - \prod_{j \in I_{\text{tangled}}} \int_{C_j^-} \left(\nabla \boldsymbol{N}_j^{-\top} \boldsymbol{D} \nabla \boldsymbol{N}_j^-\right) d\Omega, \tag{15}$$

the forcing term is given by:

$$\boldsymbol{f} = \prod_{j \in I} \int_{C_j^+} \boldsymbol{N}_j^\top b \, d\Omega - \prod_{j \in I_{\text{tangled}}} \int_{C_j^-} \boldsymbol{N}_j^{-\top} b \, d\Omega + \prod_{j \in I} \int_{\partial E_j^q} \boldsymbol{N}_j^\top q \, dS, \tag{16}$$

and, the constraint matrix by:

$$\boldsymbol{C} = \prod_{j \in I_{\text{tangled}}} \int_{F_j} [\![\boldsymbol{N}_j]\!]^\top \boldsymbol{N}^\lambda d\Omega = \prod_{j \in I_{\text{tangled}}} \int_{F_j} \left(\boldsymbol{N}_j^+ - \boldsymbol{N}_j^-\right)^\top \boldsymbol{N}^\lambda d\Omega. \tag{17}$$

Observe that the Lagrange multiplier field only needs to be square integrable since its gradient does not appear in the formulation. For Q9 elements, the primary field u is approximated using standard biquadratic functions $\boldsymbol{N}_j$, while λ is approximated using linear functions $\boldsymbol{N}^\lambda$. This choice of the $\boldsymbol{N}^\lambda$ satisfies the following conditions [9]: (a) $\boldsymbol{C}$ is full-ranked and (b)

$$n_u \geq n_\lambda \tag{18}$$

where, n_u and n_λ are the number of unknown degrees of the primary variable (u) and the Lagrange variable (λ) respectively.

4. Implementation

We now discuss the implementation of the proposed methodology.

4.1. Computing the Stiffness Matrix

Consider the two-element mesh shown in Fig. 3. Recall that the stiffness matrix is given by:

$$\boldsymbol{K} = \int\limits_{C_1^+} \left(\nabla \boldsymbol{N}_1^{+\top} \boldsymbol{D} \nabla \boldsymbol{N}_1^{+}\right) d\Omega \quad - \int\limits_{C_1^-} \left(\nabla \boldsymbol{N}_1^{-\top} \boldsymbol{D} \nabla \boldsymbol{N}_1^{-}\right) d\Omega \quad + \int\limits_{C_2^+} \left(\nabla \boldsymbol{N}_1^{+\top} \boldsymbol{D} \nabla \boldsymbol{N}_1^{+}\right) d\Omega \tag{19}$$

Since $C_2^+ = E_2$, the last term is simply the standard element stiffness matrix for that element, and can be computed numerically via standard Gauss integration, i.e.,

$$\boldsymbol{k}_2 = \int\limits_{-1}^{1}\int\limits_{-1}^{1} \left(\boldsymbol{J}^{-1}\nabla_{\boldsymbol{\xi}} \boldsymbol{N}_2\right)^{\top} \boldsymbol{D} \left(\boldsymbol{J}^{-1}\nabla_{\boldsymbol{\xi}} \boldsymbol{N}_2\right) |\boldsymbol{J}| d\xi_1 d\xi_2. \tag{20}$$

On the other hand, the first two terms in Eq. 19 are associated with the tangled element E_1. Recall that C_1^+ (C_1^-) gets mapped to the J^+ (J^-) region of the parametric space (see Fig. 2c). Accordingly, the differential area for the positive component is given by:

$$d\Omega = dx_1 dx_2 = |\boldsymbol{J}| d\xi_1 d\xi_2 \tag{21}$$

On the other hand, the differential area for the negative component is given by:

$$d\Omega = dx_1 dx_2 = -|\boldsymbol{J}| d\xi_1 d\xi_2 \tag{22}$$

Observe that since the Jacobian determinant $|\boldsymbol{J}|$ is negative, a minus sign ensures that the area remains positive.

Accordingly, the first two terms of Eq. 19 become:

$$\int\limits_{C_1^+} \left(\nabla \boldsymbol{N}_1^{+\top} \boldsymbol{D} \nabla \boldsymbol{N}_1^{+}\right) d\Omega = \int\limits_{J^+} \left(\boldsymbol{J}^{-1}\nabla_{\boldsymbol{\xi}} \boldsymbol{N}_1^{+}\right)^{\top} \boldsymbol{D} \left(\boldsymbol{J}^{-1}\nabla_{\boldsymbol{\xi}} \boldsymbol{N}_1^{+}\right) |\boldsymbol{J}| d\xi_1 d\xi_2 \tag{23}$$

and

$$\int\limits_{C_1^-} \left(\nabla \boldsymbol{N}_1^{-\top} \boldsymbol{D} \nabla \boldsymbol{N}_1^{-}\right) d\Omega = -\int\limits_{J^-} \left(\boldsymbol{J}^{-1}\nabla_{\boldsymbol{\xi}} \boldsymbol{N}_1^{-}\right)^{\top} \boldsymbol{D} \left(\boldsymbol{J}^{-1}\nabla_{\boldsymbol{\xi}} \boldsymbol{N}_1^{-}\right) |\boldsymbol{J}| d\xi_1 d\xi_2 \tag{24}$$

When these two terms are grouped together, they represent the entire parametric space of the tangled element which enables us to use the standard Gauss integration; albeit, with the sign of the Jacobian determinant included, i.e., one should not use the absolute value of the Jacobian determinant but its signed value.

$$\boldsymbol{k}_1 = \int\limits_{-1}^{1}\int\limits_{-1}^{1} \left(\boldsymbol{J}^{-1}\nabla_{\boldsymbol{\xi}} \boldsymbol{N}_1\right)^{\top} \boldsymbol{D} \left(\boldsymbol{J}^{-1}\nabla_{\boldsymbol{\xi}} \boldsymbol{N}_1\right) |\boldsymbol{J}| d\xi_1 d\xi_2. \tag{25}$$

Thus, to obtain the elemental stiffness matrix in i-TFEM, the standard Gauss integration can be employed for both regular and tangled elements, but the sign of the Jacobian must be retained. If all the Gauss points lie in the positive Jacobian region, then standard FEM is valid and there is no need for additional constraints. In many finite element implementations, the absolute value of the Jacobian determinant is used, but this will lead to erroneous results. *In addition, the constraint matrix must be included as discussed next.*

4.2. Constraint Enforcement

Next, consider the constraint matrix $\boldsymbol{C}$ in Eq. 17. For the two-element mesh (Fig. 3a), the non-zero entries of the k^{th} column of $\boldsymbol{C}$ are given by

$$\boldsymbol{C}_k = \int_{F_1} [\![\boldsymbol{N}_1(\boldsymbol{p})]\!]^\top (N^\lambda)^k(\boldsymbol{p})\, d\Omega \tag{26}$$

where $\boldsymbol{p}$ denotes a point within the fold and $(N^\lambda)^k$ is the k^{th} entry of $\boldsymbol{N}^\lambda$. This entails integrating over the fold, and can be done by triangulating the fold and evaluating the integrand at quadrature points for each triangle; see [39]. However, this is cumbersome and computationally expensive. To overcome this, an alternate method based on point collocation [9, 46] is employed here. The point collocation method leads to algebraic equations that arise in several finite element formulations [47, 48, 49, 50, 51], and will be discussed next.

Consider the 2-element mesh in Fig. 3a with one tangled element. Recall that the piecewise compatibility constraint (Eq. 3) implies that for any point $\boldsymbol{p}$ inside the fold:

$$[\![\boldsymbol{N}_1(\boldsymbol{p})]\!]\hat{\boldsymbol{u}}_1 = 0 \quad \text{i.e.,} \quad \left(\boldsymbol{N}_1^+(\boldsymbol{p}) - \boldsymbol{N}_1^-(\boldsymbol{p})\right)\hat{\boldsymbol{u}}_1 = 0 \tag{27}$$

Consider three noncollinear points ($\boldsymbol{p}_1$, $\boldsymbol{p}_2$, and $\boldsymbol{p}_3$) located in the folded region (see Fig. 4).

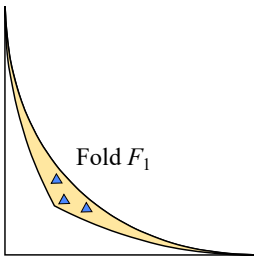

Figure 4: Three noncollinear points within the fold.

One can evaluate $[\![\boldsymbol{N}_1(\cdot)]\!]$ at these points in order to construct a matrix $\overline{\boldsymbol{C}}$ such that the non-zero entries of the k^{th} column of $\overline{\boldsymbol{C}}$ are given by

$$\overline{\boldsymbol{C}}_k = [\![\boldsymbol{N}_1(\boldsymbol{p}_k)]\!]^\top \tag{28}$$

From Eq. 27

$$\overline{\boldsymbol{C}}^\top \hat{\boldsymbol{u}} = \boldsymbol{0}. \tag{29}$$

While the two matrices $\boldsymbol{C}$ and $\overline{\boldsymbol{C}}$ are different, observe the similarities: (a) their columns are linearly independent, i.e., $\text{rank}(\overline{\boldsymbol{C}}) = \text{rank}(\boldsymbol{C}) = n_\lambda$ (= 3 in this case), and (b) they both satisfy the piecewise compatibility constraints.

We, therefore, replace the $\boldsymbol{C}$ matrix in Eq. 14 with $\overline{\boldsymbol{C}}$ to obtain a different set of Lagrange multipliers $\bar{\boldsymbol{\lambda}}$. This is acceptable since $\boldsymbol{\lambda}$ itself is not of importance here. Thus the integration over the fold can be completely avoided.

In short, for Q9 elements, the number of constraint equations is equal to 3 $\times$ degree(s) of freedom per node; these are constructed by evaluating Eq. 28 at three sample points lying in the fold. For 2D scalar (Poisson) and 2D vector (elasticity) problems, the number of constraint equations required is 3 and 6 respectively.

4.3. Multiple Overlaps

Thus far, the fold was shared by only one neighboring non-tangled element. However, in practice, the fold may be shared by multiple non-tangled elements as illustrated in Fig. 5. In this case, three non-tangled elements E_2, E_3, and E_4 overlap with element E_1 to result in the folded region F_1. However, this does not change the methodology, i.e., the stiffness matrices and constraint matrix are computed as before: (1) the standard stiffness matrices $\boldsymbol{k}_1, \boldsymbol{k}_2, \boldsymbol{k}_3, \boldsymbol{k}_4$ are computed for all elements using standard Gauss integration, and (2) the constraint matrix is computed using the entire fold F_1. The constraint matrix is constructed by evaluating Eq. 28 at (any) three points within the entire folded region.

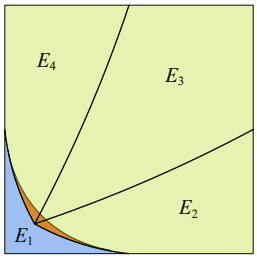

Figure 5: Fold shared by multiple non-tangled elements.

4.4. Second order triangle elements

Now consider a second order triangle (T6) element with 6-nodes (Fig. 6a). If the mid-node (p) is moved towards the left, we obtain an element with a large curvature as shown in Fig. 6b. The parametric space of this element is shown in Fig. 6c. Once the element gets tangled, the point $\boldsymbol{p}$ in the physical space can be mapped to points $\boldsymbol{a}$ and $\boldsymbol{b}$ in the negative and positive parametric region respectively. In other words, mapping is non-invertible similar to the tangled Q9 elements discussed earlier.

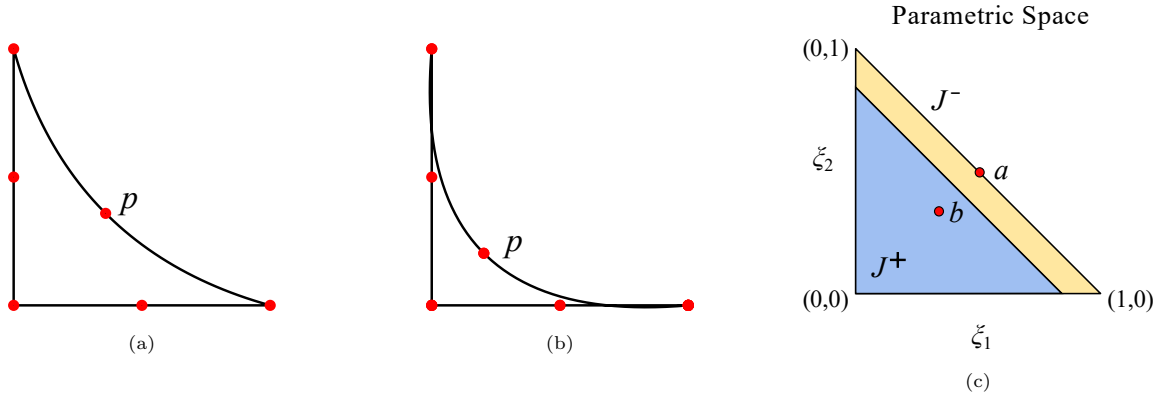

Figure 6: Quadratic triangular (T6) element (a) without tangling (b) with tangling. (c) Parametric space for the tangled element.

However, this can be handled the in same manner as in Q9 elements. The element stiffness matrices are computed while retaining the sign of the Jacobian. However, the number of constraint equations is two for T6 elements (as opposed to three for Q9 elements); this ensures that $n_u \geq n_\lambda$. Thus, to obtain the constraint matrix, we consider two points in the tangled region and evaluate Eq. 28 at these points.

4.5. Nonlinear Analysis

Next, we consider the finite elasticity problem with geometric and material nonlinearities. We employ the total Lagrangian formulation to model the deformation. Using finite element discretization, the structural equilibrium is given as

$$\boldsymbol{R}(\hat{\boldsymbol{u}}) = \boldsymbol{f}_{int} - \boldsymbol{f}_{ext} = \boldsymbol{0} \tag{30}$$

where, $\boldsymbol{f}_{ext}$ is the external nodal load vector and $\boldsymbol{f}_{int}$ is the internal nodal load vector given as:

$$\boldsymbol{f}_{int} = \frac{\partial \int_{\Omega} \Psi(\hat{\boldsymbol{u}}) d\Omega}{\partial \hat{\boldsymbol{u}}} \tag{31}$$

where Ψ is the hyperelastic strain energy density function discussed later.

In i-TFEM, the constraint matrix $\boldsymbol{C}$ is incorporated into the equilibrium equation (Eq. 30) via the Lagrange multipliers $\hat{\boldsymbol{\lambda}}$ as follows:

$$\boldsymbol{R}(\hat{\boldsymbol{u}}) + \boldsymbol{C}\hat{\boldsymbol{\lambda}} = \boldsymbol{0} \tag{32}$$

$$\boldsymbol{C}^\top \hat{\boldsymbol{u}} = \boldsymbol{0} \tag{33}$$

Due to the nonlinear nature of the problem, the equilibrium state is solved using the Newton-Raphson method where the incremental linear system of equations is given as:

$$\begin{bmatrix} \boldsymbol{K}_t & \boldsymbol{C} \\ \boldsymbol{C}^\top & \boldsymbol{0} \end{bmatrix} \begin{Bmatrix} \Delta\hat{\boldsymbol{u}}^n \\ \Delta\hat{\boldsymbol{\lambda}}^n \end{Bmatrix} = \begin{Bmatrix} -\left(\boldsymbol{R} + \boldsymbol{C}\hat{\boldsymbol{\lambda}}\right) \\ \boldsymbol{0} \end{Bmatrix}. \tag{34}$$

where $\boldsymbol{K}_t$ is the standard tangent stiffness matrix defined as

$$\boldsymbol{K}_t\left(\hat{\boldsymbol{u}}^{n-1}\right) = \partial \boldsymbol{R}(\hat{\boldsymbol{u}}^{n-1})/\partial \hat{\boldsymbol{u}}. \tag{35}$$

Then the displacements and Lagrange multipliers are updated via:

$$\hat{\boldsymbol{u}}^n = \Delta\hat{\boldsymbol{u}}^n + \hat{\boldsymbol{u}}^{n-1} \quad \text{and} \quad \hat{\boldsymbol{\lambda}}^n = \Delta\hat{\boldsymbol{\lambda}}^n + \hat{\boldsymbol{\lambda}}^{n-1}. \tag{36}$$

When the mesh is not tangled, i-TFEM reduces to the standard FEM. Thus, Eq. 34 becomes:

$$\boldsymbol{K}_t \Delta\hat{\boldsymbol{u}}^n = -\boldsymbol{R}. \tag{37}$$

A detailed discussion on the finite elements for geometric and material non-linearities can be found in [52, 53].

In Eq. 34, $\boldsymbol{K}_t$ and $\boldsymbol{R}$ are computed in the same manner as in the standard FEM, albeit, including the sign of the Jacobian determinant. The constraint matrix $\boldsymbol{C}$ can be obtained by evaluating the algebraic equations as described in Section 4.2.

5. Numerical Experiments

In this section, i-TFEM is demonstrated by solving 2D Poisson and elastostatics problems over various tangled meshes. Numerical experiments are conducted under the following conditions:

- The implementation is in MATLAB R2022a, on a standard Windows 10 desktop with Intel(R) Core(TM) i9-9820X CPU running at 3.3 GHz with 16 GB memory.
- Standard quadrature (3×3) is employed for all the elements.
- In standard FEM, the absolute value of Jacobian determinant is employed (to be consistent with commercial FEM systems such as ANSYS).

To study the rate of convergence, we define the L^2 error norm as

$$||\boldsymbol{u} - \boldsymbol{u}^h||_{L^2(\Omega)} = \left[\int_\Omega |\boldsymbol{u} - \boldsymbol{u}^h|^2 \, d\Omega\right]^{0.5} \tag{38}$$

and the energy error norm as

$$e^h = ||\nabla\boldsymbol{u} - \nabla\boldsymbol{u}^h||_{E(\Omega)} = \left[\int_\Omega \left(\nabla\boldsymbol{u} - \nabla\boldsymbol{u}^h\right)^\top \boldsymbol{D}\left(\nabla\boldsymbol{u} - \nabla\boldsymbol{u}^h\right) \, d\Omega\right]^{0.5} \tag{39}$$

where $\boldsymbol{u}$ is the reference solution and $\boldsymbol{u}^h$ is the solution under consideration.

5.1. Patch Test: Poisson problem

Consider a square domain $\Omega = (0,1) \times (0,1)$ which is discretized into four Q9 quadrilateral elements. Since we will be carrying out a patch test, Q9 elements with straight edges are considered since regular Q9 elements with curved edges (i.e., even without tangling) will not satisfy the patch test [1, 9]. The element at the bottom left corner is tangled as in Fig. 7. The folded region is shared by three neighboring non-tangled elements. We pose a Poisson problem where the exact field is given by:

$$u(x_1, x_2) = x_1^2 - x_2^2 + 3x_1 + 7x_2 - 6$$

The corresponding Dirichlet boundary conditions are imposed on all boundary edges.

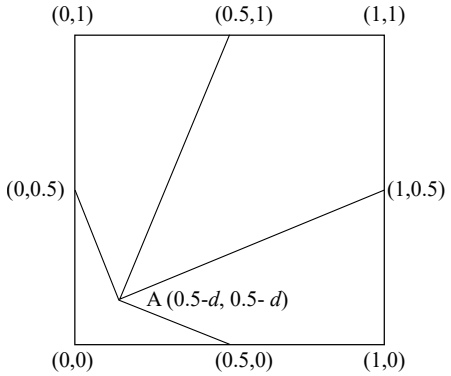

Figure 7: Tangled mesh with four elements; one of the elements is tangled.

To vary the extent of tangling, the position of node A is varied by the parameter d, where $d = 0$ corresponds to a regular mesh (4 square elements). Fig. 8a compares the L^2 errors in FEM and i-TFEM by varying d. Observe that for $d > 0.25$, the Jacobian determinant becomes negative at one or more quadrature points; consequently, FEM fails to provide accurate results. On the other hand, i-TFEM achieves machine precision accuracy even under extreme tangling. Fig. 8b shows that i-TFEM and FEM exhibit comparable condition numbers.

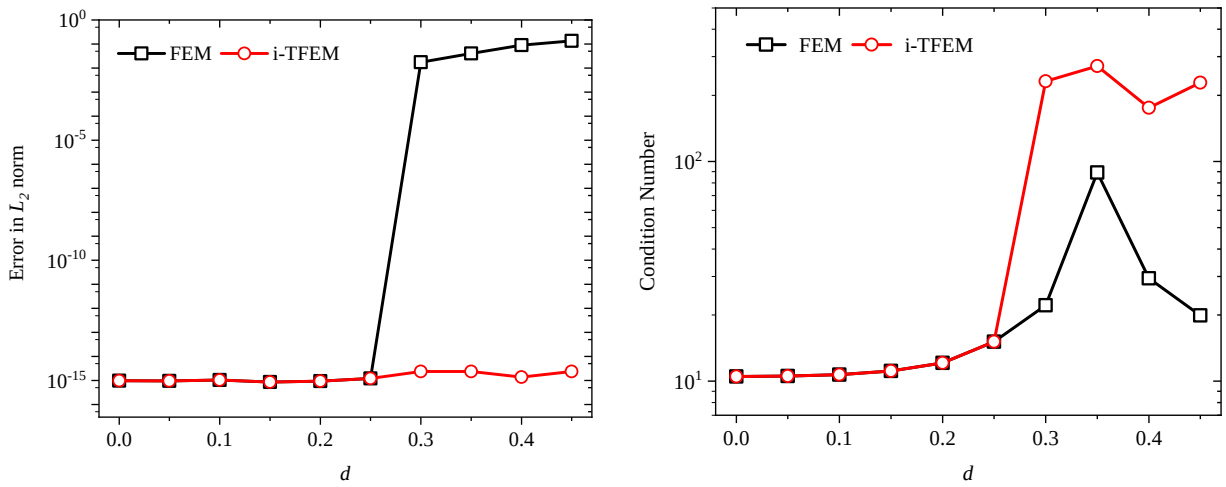

Figure 8: Comparison of i-TFEM and FEM for four-element mesh: (a) L^2 error vs. d, (b) condition number vs. d.

5.2. Patch Test: Elasticity problem

Next, we consider a cantilever subject to the loading shown in Fig. 9 [9]. The material parameters are: Young's modulus = 1000 and Poisson's ratio = 0.3; the exact displacements are quadratic fields [9].

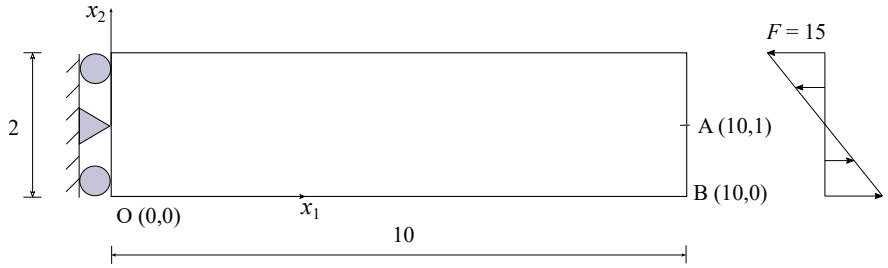

Figure 9: Cantilever bending problem.

The plane stress problem is solved over a tangled mesh shown in Fig. 10, where, once again, the degree of tangling is controlled by a parameter d.

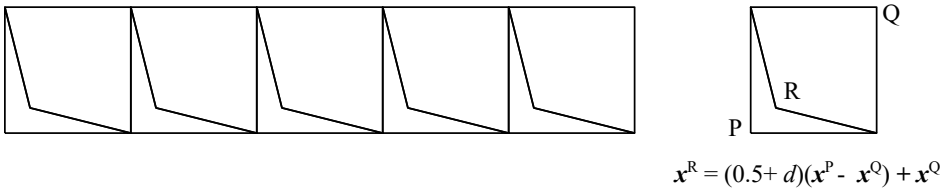

Figure 10: Tangled mesh with ten elements; five of the elements are tangled.

Fig. 11a and 11b illustrate the errors in the vertical and horizontal displacements at points A and B respectively, using FEM and i-TFEM. As in the previous example, i-TFEM achieves machine precision accuracy while classic FEM fails.

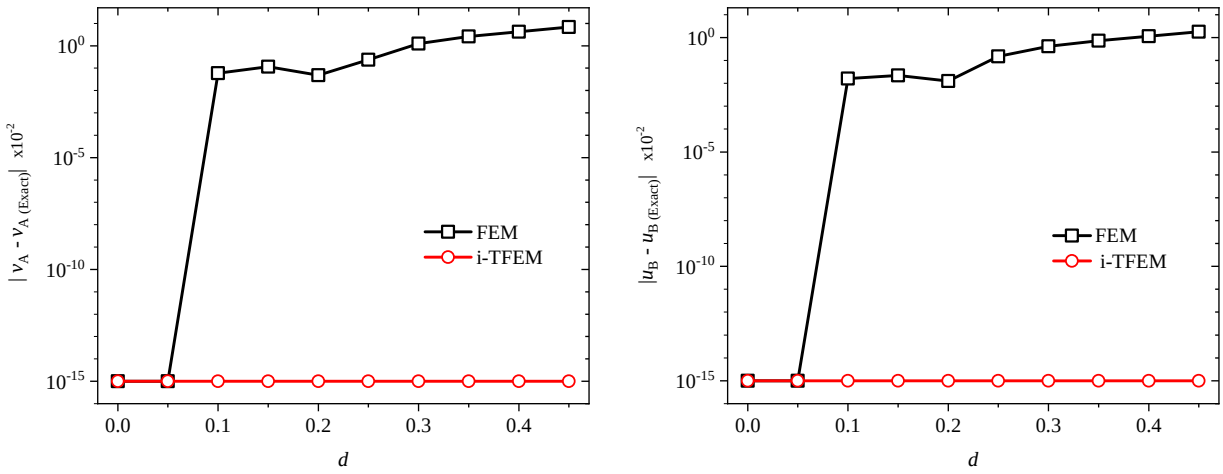

Figure 11: Comparison of i-TFEM and FEM for cantilever problem: (a) Error in vertical displacement at point A vs. d (b) Error in horizontal displacement at point B vs. d.

Fig. 12 shows that FEM and i-TFEM exhibit comparable condition numbers.

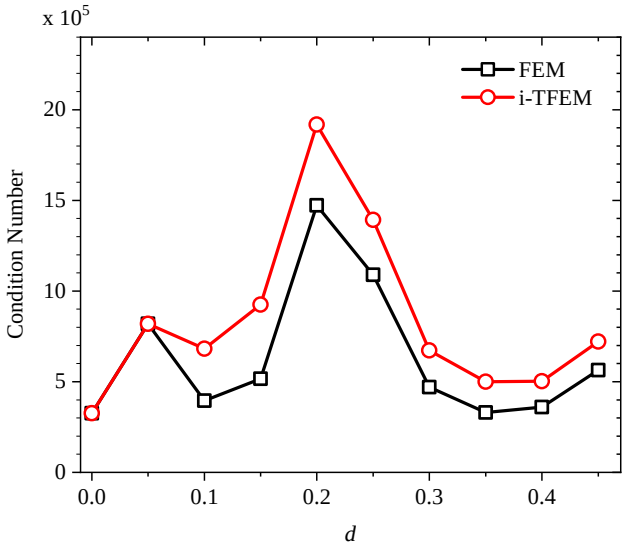

Figure 12: Condition number of FEM and i-TFEM for cantilever problem.

5.3. Cantilever with Parabolic Loading: Q9 elements

Next, we consider a plane stress cantilever problem with a parabolic vertical load P (per unit length). The load is distributed over right edge of the cantilever and $P = 1000$, $L = 48$ and $H = 12$; see Fig. 13a. The material parameters are: Young's modulus $= 3 \times 10^7$ and Poisson's ratio $= 0.3$. The boundary conditions

are applied as shown in Fig. 13a. The exact solution lies outside the FEM space and is given as [54].

$$u_1 = \frac{Px_2}{6EI}\left[(6L - 3x_1)\,x_1 + (2+\nu)\left(x_2^2 - \frac{H^2}{4}\right)\right]$$
$$u_2 = -\frac{P}{6EI}\left[(L - x_1)\,3\nu x_2^2 + (4+5\nu)\,\frac{H^2 x_1}{4} + (3L - x_1)\,x_1^2\right]$$

where $I = H^3/12$. Example of a regular mesh containing elements with curved edges is shown in Fig. 13b.

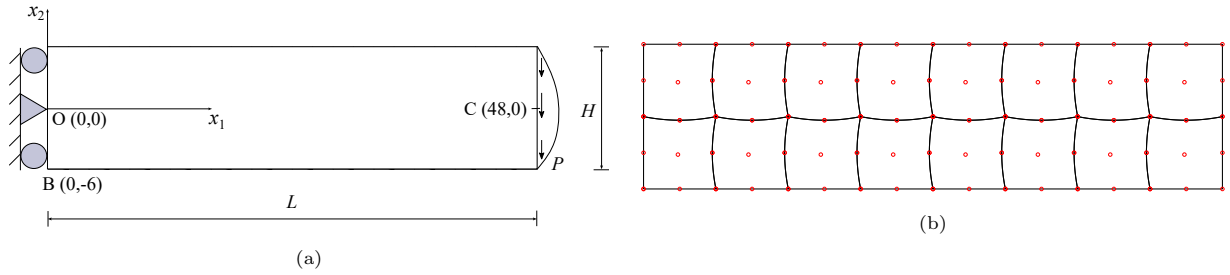

Figure 13: (a) Cantilever with parabolic loading and (b) the regular mesh.

To study the convergence for the cantilever beam problem, various tangled meshes are constructed as shown in Fig. 14.

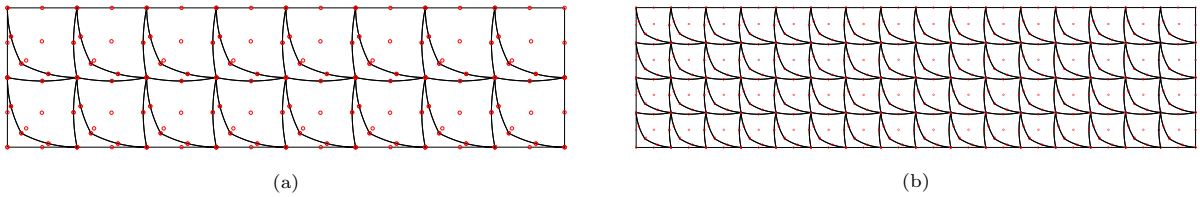

Figure 14: Sample meshes for convergence study with element size h equal to (a) 6 (b) 3.

Fig. 15a and Fig. 15b plot the L_2 and energy error norm with respect to mesh size h for the regular mesh and tangled mesh (solved using FEM and i-TFEM) containing curved elements. Observe that the convergence rates over tangled mesh obtained via i-TFEM and over the regular mesh are similar.

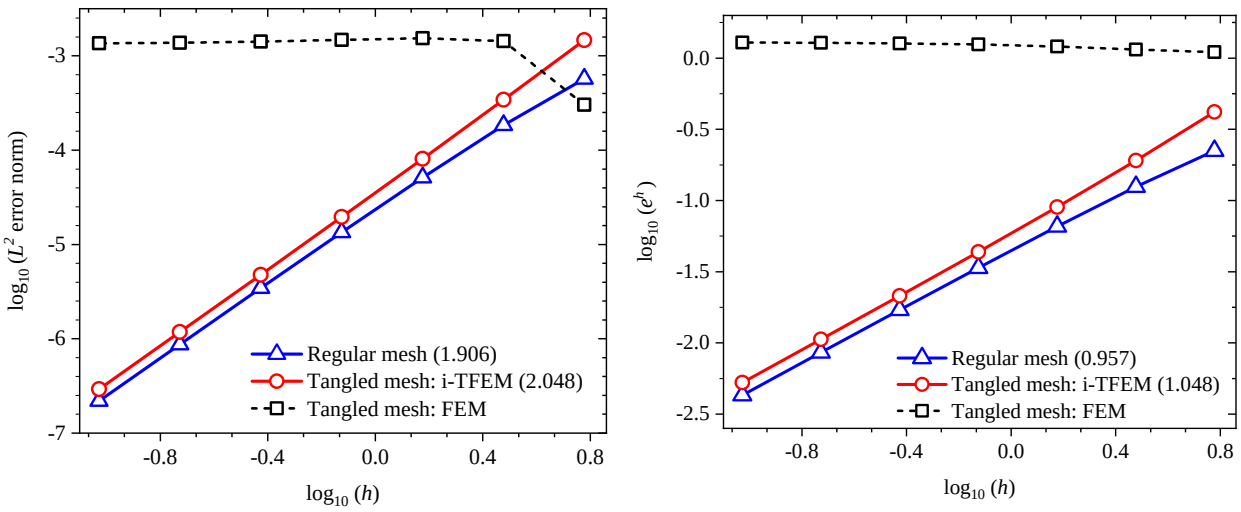

(a) (b)

Figure 15: (a) L^2 and (b) energy norm errors as a function of the element size h for cantilever problem with curved Q9 elements. Convergence rates are provided in parenthesis.

5.4. Cantilever with Parabolic Loading: Quadratic triangular (T6) elements

Next, we consider the mesh with quadratic triangular elements. An example of a regular mesh and a tangled mesh containing elements with curved edges is shown in Fig. 16.

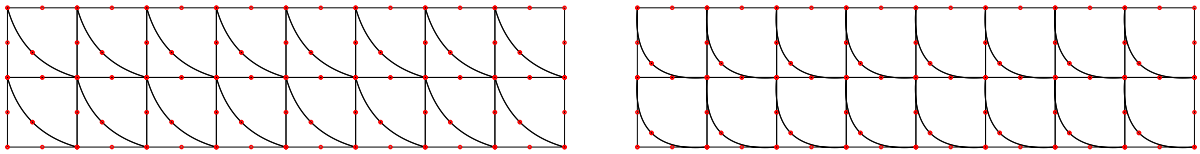

(a) (b)

Figure 16: (a) Regular and (b) tangled meshes containing T6 elements with curved sides; $h = 6$.

To study the convergence properties of i-TFEM, the cantilever problem with parabolic loading previously discussed in Section 5.3 is solved over the regular and tangled mesh using i-TFEM and FEM. Fig. 17a and Fig. 17b plot the L_2 and energy error norms vs mesh size h. Once again, the convergence rate of i-TFEM over the tangled mesh is similar to that of FEM over the regular mesh.

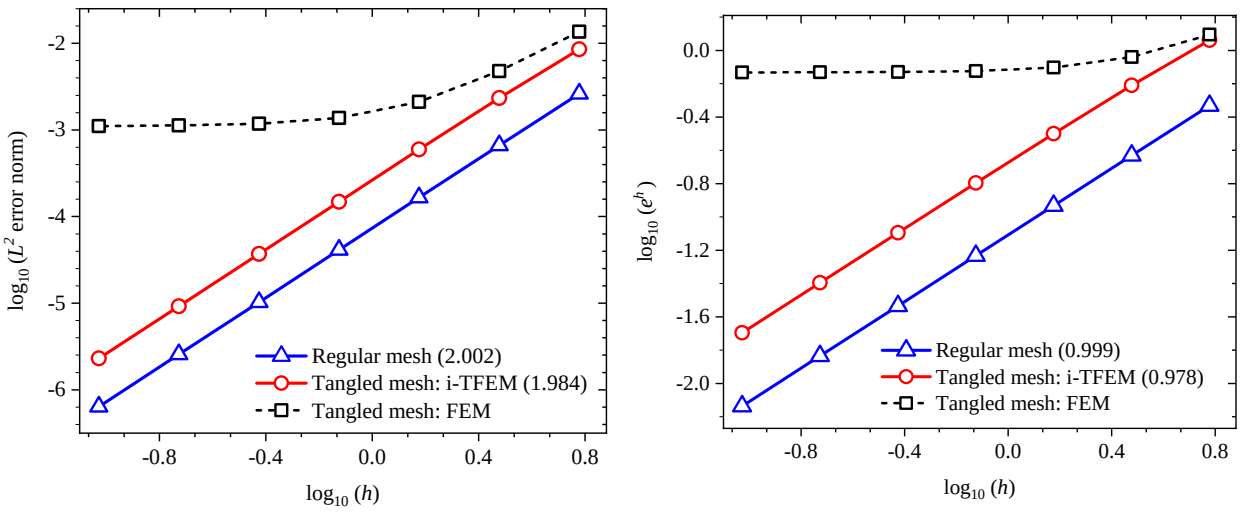

(a) (b)

Figure 17: (a) L^2 and (b) energy norm errors as a function of the element size h for cantilever problem with T6 elements. The convergence rates are provided in the brackets.

5.5. Mesh Morphing with Q9 elements

Consider *mesh morphing* where the mesh is updated under geometric changes by simply moving the mesh nodes according to a specified rule [21] (rather than regenerating the mesh which can change the underlying mesh topology). As an example, consider the domain in Fig. 18a, with the initial mesh as illustrated in Fig. 18b.

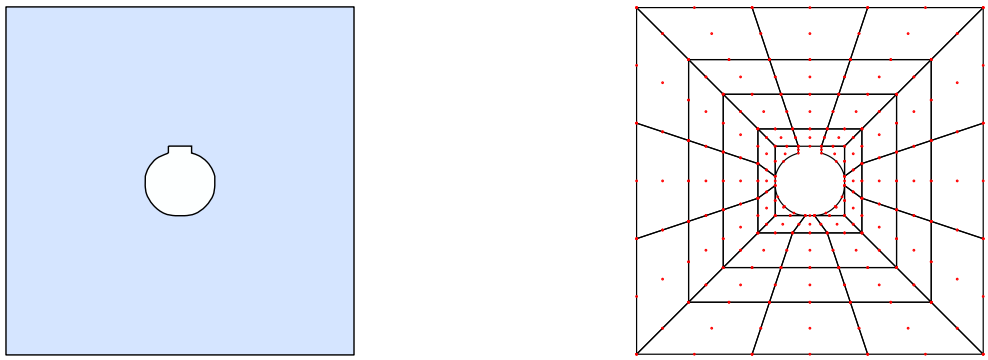

(a) (b)

Figure 18: (a) Domain and (b) Initial mesh containing Q9 elements.

The inner boundary is now rotated in a counterclockwise direction by an angle β, and the mesh is morphed as follows. All nodes except the outer boundary nodes are rotated about the center such that the angle of rotation exponentially increase from 0° to β as nodes get closer to the void. Fig. 19 illustrates the morphed mesh for $\beta = 70^\circ$. Observe that some quads (shown in red) are tangled, i.e., the mesh is tangled.

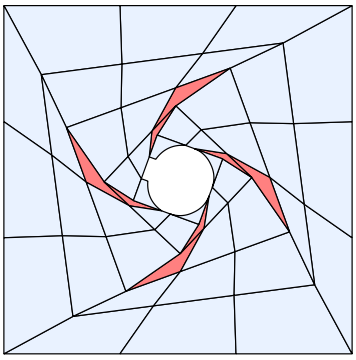

Figure 19: Morphed mesh for $\beta = 70°$.

We solve the Poisson problem using i-TFEM with the zero (homogenous) Dirichlet condition applied on the entire boundary and the source term set to $b(x_1, x_2) = 1$. Fig. 20 illustrates the post-processed results for $\beta = 0°,\ 40°$, and $70°$.

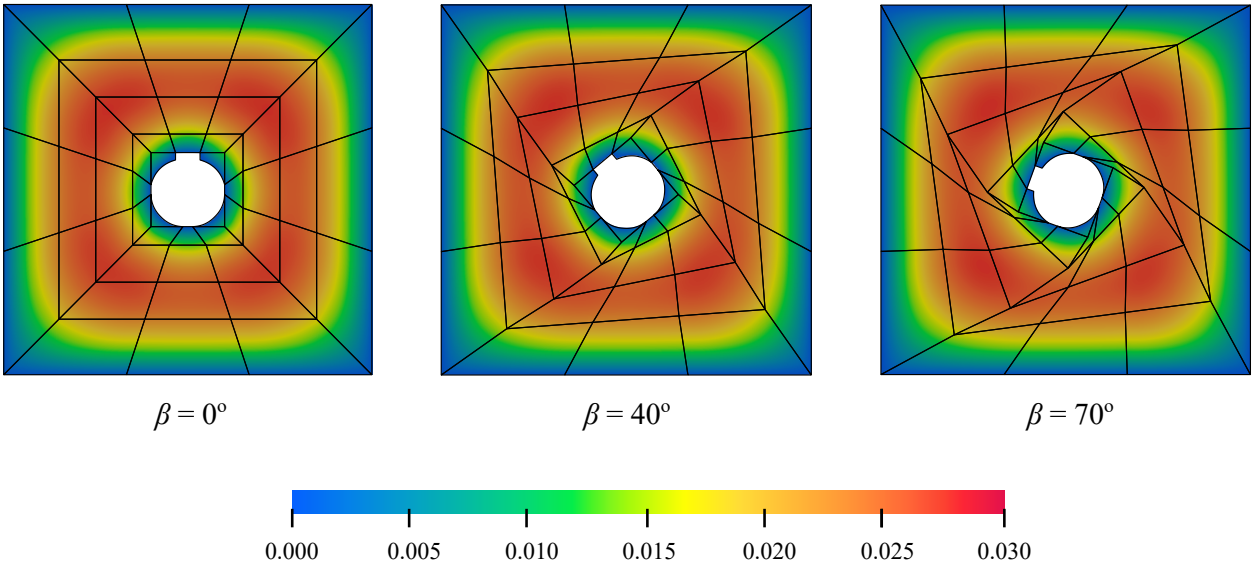

Figure 20: Post-processed solution using i-TFEM for morphed meshes.

5.6. Disc with T6 elements

Consider the T6 mesh illustrated earlier in Fig. 1d where two (out of 295) elements, shown in red color, are tangled. Though it is possible to untangle this mesh [22], i-TFEM completely eliminates the need for untangling. Here, we compare the results for tangled and untangled meshes.

An elastostatics plane stress problem is set up with the following boundary conditions: homogeneous Dirichlet boundary condition is applied on the outer boundary while a counterclockwise torque $= 1 \times 10^9$ is applied on the innermost circular boundary. The problem is solved using i-TFEM over the tangled mesh with material parameters $E = 2 \times 10^{11}$ and Poisson's ratio $= 0.3$. Fig. 21a and Fig. 21b illustrate the displacement field for the tangled mesh (using i-TFEM) untangled mesh. i-TFEM required 1.200 milliseconds while FEM

required 1.199 milliseconds to solve the problem.

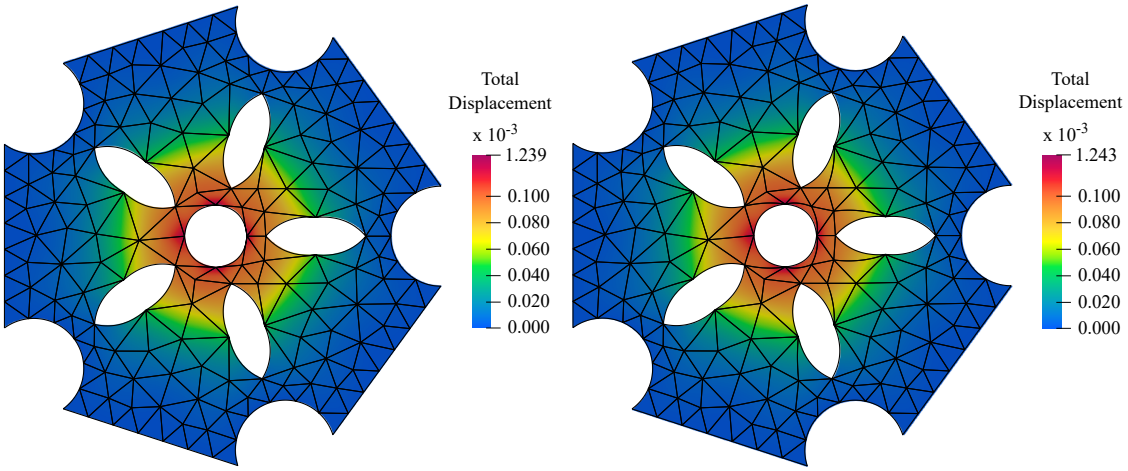

(a) (b)

Figure 21: (a) Displacement field obtained using i-TFEM (c) Displacement field using untangled mesh. Both meshes were provided by the authors of [22].

5.7. Nonlinear Punch Problem

To evaluate the performance of i-TFEM in the presence of geometric and material nonlinearities, we consider the punch problem [55, 56, 33, 57]. A rectangular block is subject to a vertical load p (per unit length) uniformly distributed over the top left half of the block where $p = 1000$ and $H = 1$; see Fig. 22 [33]. The top and left sides of the block are fixed in the horizontal direction, while the bottom is fixed in the vertical direction. The domain is meshed using Q9 elements with curved edges. The mesh size is governed by the index N where the number of elements in the regular mesh is $2^{N+1} \times 2^N$. The regular and tangled meshes with $N = 2$ are shown in Fig. 22. Observe the elements in both meshes have curved edges.

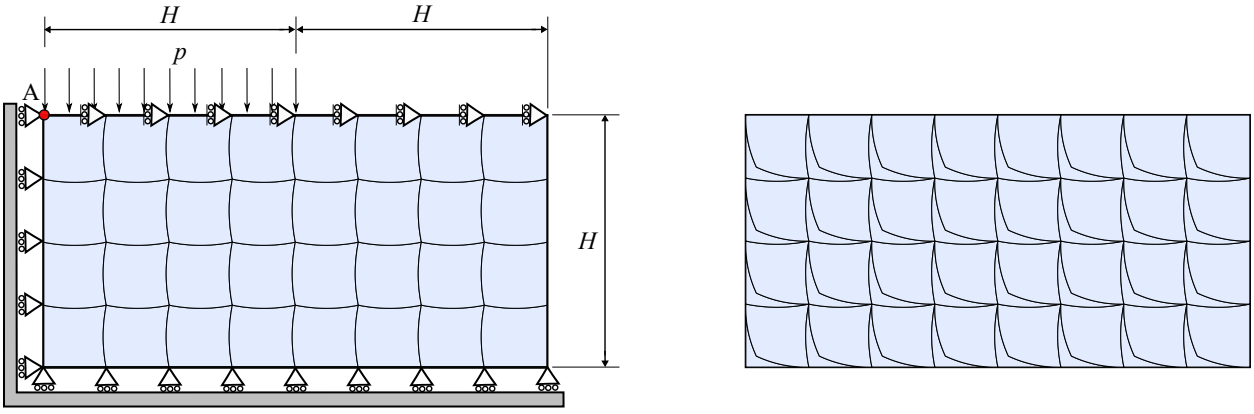

Figure 22: Initial configuration of the punch problem with mesh size $N = 2 \equiv 8 \times 4$ and the tangled Q9 mesh.

The problem is solved over these meshes (using i-TFEM and FEM) assuming plane strain condition and hyperelastic material model. Specifically, we employ the compressible isotropic generalized neo-Hookean

material model where the strain energy density is given by [52, 53]:

$$\Psi_{\text{GNH}}(\boldsymbol{u}) = \frac{\mu}{2}\left(J_F^{-2/3} tr\boldsymbol{b} - 3\right) + \frac{K}{2}\left(J_F - 1\right)^2. \tag{40}$$

Here, $J_F = det\boldsymbol{F}$, $\boldsymbol{b} = \boldsymbol{F}\boldsymbol{F}^\top$ is the left Cauchy-Green deformation tensor, and $\boldsymbol{F}$ is the deformation gradient. Here, $\mu = 500$ and $K = 1700$ are the material parameters (equivalent to shear and bulk moduli respectively in the small strain limit). Deformed configurations for untangled and tangled obtained (via i-TFEM) meshes are shown in Fig. 23.

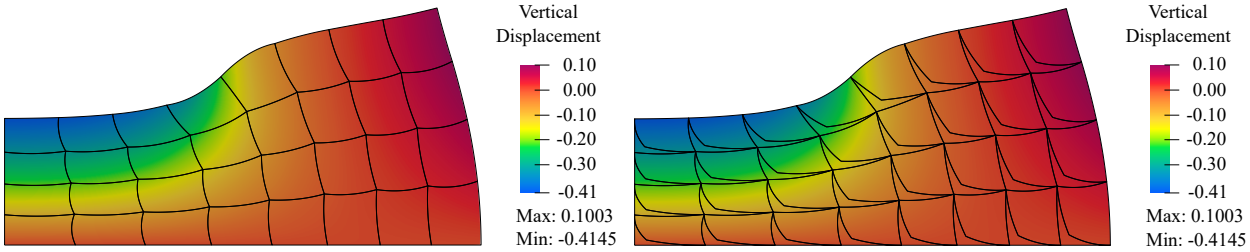

(a) (b)

Figure 23: Deformed configuration for (a) regular mesh via FEM and (b) tangled mesh via i-TFEM for the punch problem.

Further, a convergence study was then carried out as N was varied. The vertical displacement u_2 at the top-left corner point A for the two methods is plotted against the mesh index N in Fig. 24. One can observe that the solutions obtained by FEM over the regular mesh and i-TFEM over the tangled mesh converge to the same solution while standard FEM over the tangled mesh converges to an incorrect solution.

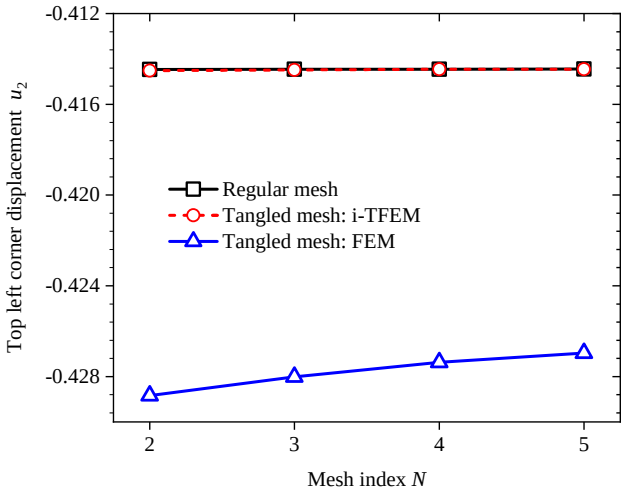

Figure 24: Convergence study for the punch problem.

5.8. Need for constraints

Recall that i-TFEM requires enforcement of the constraint equations. We emphasize the importance of constraints through illustrative examples. Consider the nonlinear elasticity problem discussed in Section 5.7. If the problem is solved without the constraints, Newton-Raphson diverges.

As another example, consider a long hollow cylinder with internal radius $a = 1$ and external radius $b = 4$; see Fig. 25a. A uniform pressure $p = 1$ is applied to the inner surface ($r = a$) and the cylinder deforms in plane strain. Let the Poisson's ratio, $\nu = 0.3$ and Young's modulus, $E = 2.6$. Due to the axisymmetric nature of the problem, only a quarter of the cylinder is modeled. The analytical solution is as follows [54]:

$$\boldsymbol{u} = \frac{p(1+\nu)a^2b^2}{E(b^2-a^2)}\left(\frac{1}{r} + \frac{r(1-2\nu)}{b^2}\right)\boldsymbol{e}_r$$

A typical 4-node quadrilateral mesh, shown in Fig. 25b, is constructed by using the two-element mesh as the basic repeating unit.

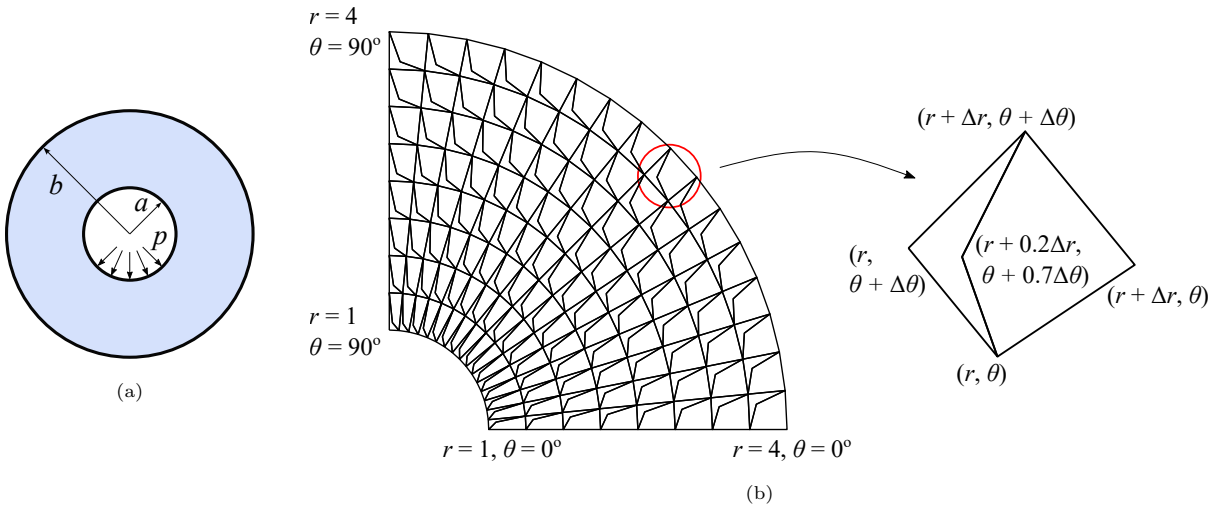

Figure 25: (a) Cross-section of the pressurized cylinder (b) A typical mesh with tangled elements.

Fig. 26a and Fig. 26b respectively illustrate the radial stress distribution, with and without compatibility constraints. Similarly, Fig. 27a and Fig. 27b respectively show the displacement field obtained with and without incorporating the compatibility constraints. The solutions are plotted over the undeformed mesh. The results produced by the two methods are quite different; the one without constraints leads to unacceptable results; Fig. 28 illustrates the deformed mesh. Thus, erroneous or even nonsensical results may be produced in the absence of constraint equations.

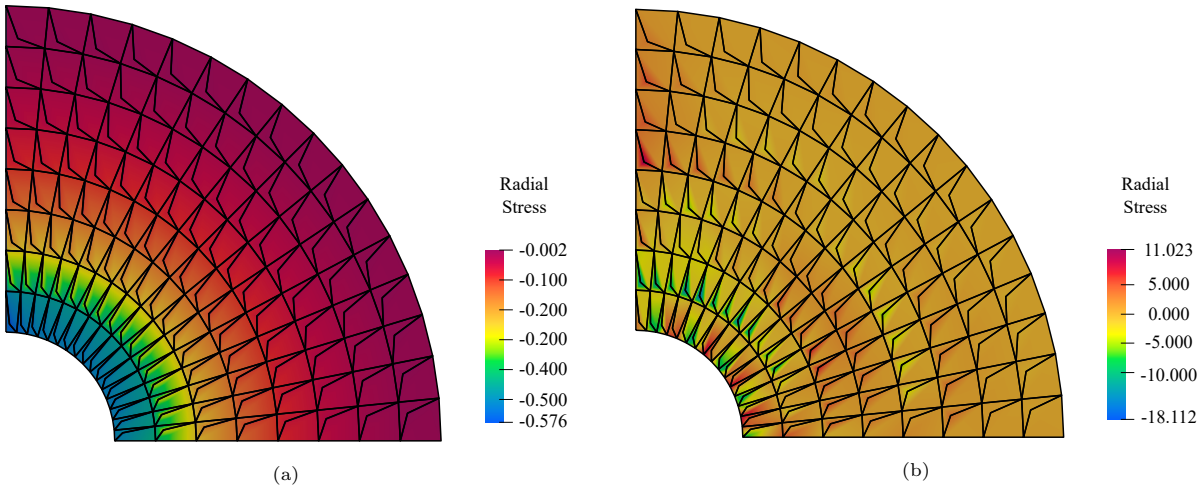

(a) (b)

Figure 26: Radial stress distribution for the pressurized cylinder problem (a) with and (b) without the compatibility constraints plotted over underformed mesh.

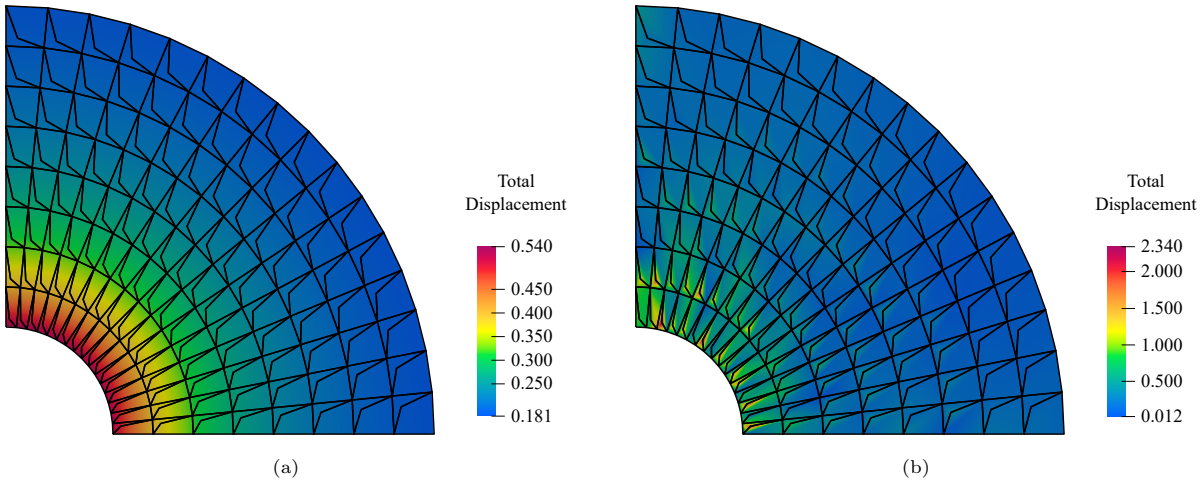

(a) (b)

Figure 27: Displacement field for the pressurized cylinder problem (a) with and (b) without the compatibility constraints plotted over un-deformed mesh.

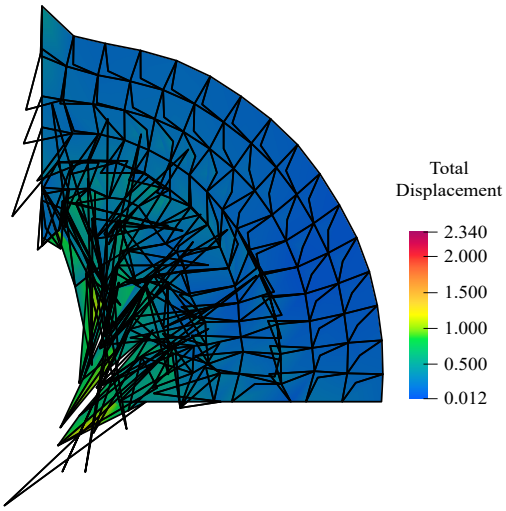

Figure 28: Deformed configuration for the pressurized cylinder problem without the compatibility constraints.

6. Conclusions

When the mesh contains tangled elements, the parametric mapping is non-injective, leading to erroneous results in standard FEM. The paper presents a novel method for handling such elements. The proposed isoparametric tangled finite element method (i-TFEM) is demonstrated for 9-node quadrilateral and 6-node triangular elements. The features of the proposed method are:

1. The variational functional can be obtained by modifying the standard potential energy functional by (a) treating the positive and negative components separately and (b) incorporating compatibility constraints. Consequently, the full-invertibility requirement is replaced by piecewise invertibility.

2. The stiffness matrix can be computed as in standard FEM, but the sign of the Jacobian determinant must be retained during integration.

3. To enforce compatibility over the fold, a constraint matrix $\boldsymbol{C}$ must be constructed by sampling the shape functions at n_c points within the fold, where $n_c = 2$ for a T6 element and $n_c = 3$ for a Q9 element. Thus, every tangled element adds n_c degrees of freedom for 2D scalar problems and $2n_c$ for 2D vector (elasticity) problems.

4. Consequently, to implement i-TFEM, only two changes need to made to an existing FEM code: (a) retain the Jacobian determinant sign and (b) incorporate the algebraic constraint equations. The symmetry of the resulting linear system of equations is retained.

5. Finally, i-TFEM reduces to the standard FEM when the mesh is regular.

Further, numerous examples are presented to demonstrate the effectiveness of the proposed method. Linear and nonlinear elasticity as well as Poisson problems are solved over non-tangled and tangled meshes using i-TFEM and FEM. From the numerical experiments, we observe that:

6. The accuracy and convergence rate (with respect to L_2 and energy error norms) of i-TFEM over a tangled mesh is comparable to that of the standard FEM over a non-tangled mesh. On the other hand, FEM over tangled mesh results in inaccurate results.

7. For nonlinear analysis, i-TFEM over the tangled mesh converges to the same solution as obtained over the non-tangled mesh.

8. FEM and i-TFEM exhibit comparable condition numbers.

9. The time required for i-TFEM is almost identical to that for standard FEM in practical scenarios.

Future work will focus on extending i-TFEM to higher order 3D elements [23, 15, 58, 22] as well as isogeometric analysis [59] where tangling is known to occur [60, 61, 20], and leads to erroneous results. While the condition numbers for i-TFEM and FEM were found to be comparable, a detailed stability analysis is desirable, and will be carried out in the future.

Acknowledgments

The authors would like to thank the support of National Science Foundation through grant 1715970. We would also to thank Prof. Suzanne Shontz for providing the tangled and untangled meshes.

Appendix A. Identification of the positive and negative Jacobian regions

While the proposed i-TFEM implementation does not require explicit identification of the J^+ and J^- regions, for completeness, we provide here a procedure for identifying these two regions.

Recall that the determinant of the Jacobian associated with isoparametric mapping is given by:

$$|\boldsymbol{J}| = \begin{vmatrix} x(\xi,\eta)_{,\xi} & y(\xi,\eta)_{,\xi} \\ x(\xi,\eta)_{,\eta} & y(\xi,\eta)_{,\eta} \end{vmatrix} \tag{A.1}$$

When an element becomes tangled, the parametric space can be decomposed into a positive $|\boldsymbol{J}|$ region and a negative $|\boldsymbol{J}|$ region, denoted as J^+ and J^- respectively. The two regions are divided by the $|\boldsymbol{J}| = 0$ curve, i.e., we can identify the J^+ and J^- regions by computing the $|\boldsymbol{J}| = 0$ curve.

To illustrate, we consider a 4-noded bilinear quadrilateral (Q4) element for simplicity. Let the element be defined by the vertices $[(x_1, y_1), (x_2, y_2), (x_3, y_3), (x_4, y_4)]$. Given the bilinear mapping, the Jacobian is given by

$$\boldsymbol{J} = \frac{1}{4} \begin{bmatrix} \eta - 1 & 1 - \eta & 1 + \eta & -(1+\eta) \\ \xi - 1 & -(1+\xi) & 1 + \xi & 1 - \xi \end{bmatrix} \begin{bmatrix} x_1 & x_2 & x_3 & x_4 \\ y_1 & y_2 & y_3 & y_4 \end{bmatrix}^T$$

The Jacobian determinant can be expressed as a straight line:

$$|\boldsymbol{J}| = \det(\boldsymbol{J}) = c_0 + c_1\xi + c_2\eta \tag{A.2}$$

where,

$$c_0 = [(x_1 - x_3)(y_2 - y_4) - (x_2 - x_4)(y_1 - y_3)]/8,$$
$$c_1 = [(x_3 - x_4)(y_1 - y_2) - (x_1 - x_2)(y_3 - y_4)]/8,$$
$$c_2 = [(x_2 - x_3)(y_1 - y_4) - (x_1 - x_4)(y_2 - y_3)]/8.$$

Thus, the two regions can be computed easily.

For a 9-node quadrilateral (Q9) element, the $|\boldsymbol{J}| = 0$ is no longer a straight line. However, it is possible to derive an expression for this curve. For example, one can show that, for the tangled Q9 element in Fig. 2b, the $|\boldsymbol{J}| = 0$ curve is given by

$$0.0605\xi^2\eta^2 - 0.0055\left(\xi^2\eta + \xi\eta^2\right) - 0.0129\left(\xi^2 + \eta^2\right) - 3.1762\left(\xi + \eta\right) + 1.2898\xi\eta + 1.2127 = 0.$$

Consequently, one can identify the two regions J^+ and J^-.

References

[1] R. D. Cook, et al., Concepts and applications of finite element analysis, John wiley & sons, 2007.

[2] X. Cui, S. Duan, S. Huo, G. Liu, A high order cell-based smoothed finite element method using triangular and quadrilateral elements, Engineering Analysis with Boundary Elements 128 (2021) 133–148.

[3] C. Manu, Complete quadratic isoparametric finite elements in fracture mechanics analysis, International journal for numerical methods in engineering 21 (8) (1985) 1547–1553.

[4] M.-C. Trinh, H. Jun, A higher-order quadrilateral shell finite element for geometrically nonlinear analysis, European Journal of Mechanics-A/Solids 89 (2021) 104283.

[5] A. Masud, R. Khurram, A multiscale finite element method for the incompressible navier–stokes equations, Computer Methods in Applied Mechanics and Engineering 195 (13-16) (2006) 1750–1777.

[6] D. Hendriana, K. J. Bathe, On a parabolic quadrilateral finite element for compressible flows, Computer Methods in Applied Mechanics and Engineering 186 (1) (2000) 1–22.

[7] A. C. Polycarpou, Introduction to the finite element method in electromagnetics, Synthesis Lectures on Computational Electromagnetics 1 (1) (2005) 1–126.

[8] L. Huang, R. Mandeville, W. Rolph III, Magnetostatics and coupled structural finite element analysis, Computers & structures 72 (1-3) (1999) 199–207.

[9] O. C. Zienkiewicz, R. L. Taylor, J. Z. Zhu, The finite element method: its basis and fundamentals, Elsevier, 2005.

[10] P. J. Frey, P.-L. George, Mesh generation: application to finite elements, Iste, 2007.

[11] D. S. Lo, Finite element mesh generation, CRC Press, 2014.

[12] T. Blacker, Automated conformal hexahedral meshing constraints, challenges and opportunities, Engineering with Computers 17 (3) (2001) 201–210.

[13] N. Pietroni, M. Campen, A. Sheffer, G. Cherchi, D. Bommes, X. Gao, R. Scateni, F. Ledoux, J.-F. Remacle, M. Livesu, Hex-mesh generation and processing: a survey, ACM Transactions on Graphics (TOG) (2022).

[14] M. N. Akram, L. Si, G. Chen, An embedded polygon strategy for quality improvement of 2d quadrilateral meshes with boundaries., in: VISIGRAPP (1: GRAPP), 2021, pp. 177–184.

[15] J.-F. Remacle, T. Toulorge, J. Lambrechts, Robust untangling of curvilinear meshes, in: Proceedings of the 21st International meshing roundtable, Springer, 2013, pp. 71–83.

[16] L. A. Freitag, P. Plassmann, Local optimization-based simplicial mesh untangling and improvement, International Journal for Numerical Methods in Engineering 49 (1-2) (2000) 109–125.

[17] P. M. Knupp, Achieving finite element mesh quality via optimization of the jacobian matrix norm and associated quantities. part ii—a framework for volume mesh optimization and the condition number of the jacobian matrix, International Journal for numerical methods in engineering 48 (8) (2000) 1165–1185.

[18] J. M. Escobar, E. Rodrıguez, R. Montenegro, G. Montero, J. M. González-Yuste, Simultaneous untangling and smoothing of tetrahedral meshes, Computer Methods in Applied Mechanics and Engineering 192 (25) (2003) 2775–2787.

[19] P. M. Knupp, A method for hexahedral mesh shape optimization, International journal for numerical methods in engineering 58 (2) (2003) 319–332.

[20] D. Fußeder, B. Simeon, A.-V. Vuong, Fundamental aspects of shape optimization in the context of isogeometric analysis, Computer Methods in Applied Mechanics and Engineering 286 (2015) 313–331.

[21] M. L. Staten, S. J. Owen, S. M. Shontz, A. G. Salinger, T. S. Coffey, A comparison of mesh morphing methods for 3d shape optimization, in: Proceedings of the 20th international meshing roundtable, Springer, 2011, pp. 293–311.

[22] M. Stees, M. Dotzel, S. M. Shontz, Untangling high-order meshes based on signed angles, Proceedings of the 28th International Meshing Roundtable (2020).

[23] M. Stees, S. M. Shontz, An angular approach to untangling high-order curvilinear triangular meshes, in: International Meshing Roundtable, Springer, 2018, pp. 327–342.

[24] T. Toulorge, C. Geuzaine, J.-F. Remacle, J. Lambrechts, Robust untangling of curvilinear meshes, Journal of Computational Physics 254 (2013) 8–26.

[25] X. Roca, A. Gargallo-Peiró, J. Sarrate, Defining quality measures for high-order planar triangles and curved mesh generation, in: Proceedings of the 20th International Meshing Roundtable, Springer, 2012, pp. 365–383.

[26] E. Ruiz-Gironés, J. Sarrate, X. Roca, Generation of curved high-order meshes with optimal quality and geometric accuracy, Procedia engineering 163 (2016) 315–327.

[27] F. Mohammadi, S. Dangi, S. M. Shontz, C. A. Linte, A direct high-order curvilinear triangular mesh generation method using an advancing front technique, in: International Conference on Computational Science, Springer, 2020, pp. 72–85.

[28] J. Sarrate, A. Huerta, Efficient unstructured quadrilateral mesh generation, International journal for numerical methods in engineering 49 (10) (2000) 1327–1350.

[29] G. Liu, K. Dai, T. T. Nguyen, A smoothed finite element method for mechanics problems, Computational Mechanics 39 (6) (2007) 859–877.

[30] L. Beirão da Veiga, F. Brezzi, A. Cangiani, G. Manzini, L. D. Marini, A. Russo, Basic principles of virtual element methods, Mathematical Models and Methods in Applied Sciences 23 (01) (2013) 199–214.

[31] L. B. Da Veiga, F. Dassi, A. Russo, High-order virtual element method on polyhedral meshes, Computers & Mathematics with Applications 74 (5) (2017) 1110–1122.

[32] E. Artioli, L. B. Da Veiga, F. Dassi, Curvilinear virtual elements for 2d solid mechanics applications, Computer Methods in Applied Mechanics and Engineering 359 (2020) 112667.

[33] M. De Bellis, P. Wriggers, B. Hudobivnik, Serendipity virtual element formulation for nonlinear elasticity, Computers & Structures 223 (2019) 106094.

[34] S. P. Bordas, S. Natarajan, P. Kerfriden, C. E. Augarde, D. R. Mahapatra, T. Rabczuk, S. D. Pont, On the performance of strain smoothing for quadratic and enriched finite element approximations (xfem/gfem/pufem), International Journal for Numerical Methods in Engineering 86 (4-5) (2011) 637–666.

[35] S. Rajendran, A technique to develop mesh-distortion immune finite elements, Computer Methods in Applied Mechanics and Engineering 199 (17-20) (2010) 1044–1063.

[36] B. Prabhune, K. Suresh, A computationally efficient isoparametric tangled finite element method for handling inverted quadrilateral and hexahedral elements, Computer Methods in Applied Mechanics and Engineering 405 (2023) 115897.

[37] B. Prabhune, K. Suresh, Towards tangled finite element analysis over partially inverted hexahedral elements, arXiv preprint arXiv:2207.03905 (2022).

[38] B. Prabhune, K. Suresh, Isoparametric tangled finite element method for nonlinear elasticity, arXiv preprint arXiv:2303.10799 (2023).

[39] B. Prabhune, S. Sridhara, K. Suresh, Tangled finite element method for handling concave elements in quadrilateral meshes, International Journal for Numerical Methods in Engineering 123 (7) (2022) 1576–1605.

[40] B. Dhas, A. R. Srinivasa, J. Reddy, D. Roy, A novel four-field mixed fe approximation for kirchhoff rods using cartan's moving frames, Computer Methods in Applied Mechanics and Engineering (2022) 115094.

[41] T. H. Pian, Finite element formulation by variational principles with relaxed continuity requirements, in: The mathematical foundations of the finite element method with applications to partial differential equations, Elsevier, 1972, pp. 671–687.

[42] P. Tong, New displacement hybrid finite element models for solid continua, International Journal for Numerical Methods in Engineering 2 (1) (1970) 73–83.

[43] C. Farhat, F.-X. Roux, A method of finite element tearing and interconnecting and its parallel solution algorithm, International journal for numerical methods in engineering 32 (6) (1991) 1205–1227.

[44] J. T. Oden, J. N. Reddy, Variational methods in theoretical mechanics, Springer Science & Business Media, 2012.

[45] F. Auricchio, L. B. da Veiga, F. Brezzi, C. Lovadina, Mixed finite element methods, Encyclopedia of Computational Mechanics Second Edition (2017) 1–53.

[46] E. Oñate, S. Idelsohn, O. Zienkiewicz, R. Taylor, A finite point method in computational mechanics. applications to convective transport and fluid flow, International journal for numerical methods in engineering 39 (22) (1996) 3839–3866.

[47] R. Kramer, P. Bochev, C. Siefert, T. Voth, An extended finite element method with algebraic constraints (xfem-ac) for problems with weak discontinuities, Computer Methods in Applied Mechanics and Engineering 266 (2013) 70–80.

[48] R. M. Kramer, P. B. Bochev, C. M. Siefert, T. E. Voth, Algebraically constrained extended edge element method (exfem-ac) for resolution of multi-material cells, Journal of Computational Physics 276 (2014) 596–612.

[49] R. M. Kramer, C. M. Siefert, T. E. Voth, P. B. Bochev, Formulation and computation of dynamic, interface-compatible whitney complexes in three dimensions, Journal of Computational Physics 359 (2018) 45–76.

[50] G. J. Wagner, W. K. Liu, Application of essential boundary conditions in mesh-free methods: a corrected collocation method, International Journal for Numerical Methods in Engineering 47 (8) (2000) 1367–1379.

[51] C.-K. C. Wu, M. E. Plesha, Essential boundary condition enforcement in meshless methods: boundary flux collocation method, International Journal for Numerical methods in engineering 53 (3) (2002) 499–514.

[52] O. C. Zienkiewicz, R. L. Taylor, R. L. Taylor, The finite element method: solid mechanics, Vol. 2, Butterworth-heinemann, 2000.

[53] A. F. Bower, Applied mechanics of solids, CRC press, 2009.

[54] S. Timoshenko, J. Goodier, Theory of elasticity 3rd ed., 567 (1970).

[55] P. Wriggers, B. Reddy, W. Rust, B. Hudobivnik, Efficient virtual element formulations for compressible and incompressible finite deformations, Computational Mechanics 60 (2017) 253–268.

[56] Z. Li, S. Cen, J. Huang, C.-F. Li, Hyperelastic finite deformation analysis with the unsymmetric finite element method containing homogeneous solutions of linear elasticity, International Journal for Numerical Methods in Engineering 121 (16) (2020) 3702–3721.

[57] D. van Huyssteen, B. D. Reddy, A virtual element method for isotropic hyperelasticity, Computer Methods in Applied Mechanics and Engineering 367 (2020) 113134.

[58] D. Moxey, M. Green, S. Sherwin, J. Peiró, An isoparametric approach to high-order curvilinear boundary-layer meshing, Computer Methods in Applied Mechanics and Engineering 283 (2015) 636–650.

[59] T. J. Hughes, J. A. Cottrell, Y. Bazilevs, Isogeometric analysis: Cad, finite elements, nurbs, exact geometry and mesh refinement, Computer methods in applied mechanics and engineering 194 (39-41) (2005) 4135–4195.

[60] S. Xia, X. Qian, Generating high-quality high-order parameterization for isogeometric analysis on triangulations, Computer Methods in Applied Mechanics and Engineering 338 (2018) 1–26.

[61] G. Xu, B. Mourrain, R. Duvigneau, A. Galligo, Parameterization of computational domain in isogeometric analysis: methods and comparison, Computer Methods in Applied Mechanics and Engineering 200 (23-24) (2011) 2021–2031.